

Moiré superlattice on the surface of Sm films driven by surface valence transition

Jianzhou Bian(边建州), Hao Zheng(郑浩), Yonghao Liu(刘永昊), Zongxiu Wu(邬宗秀), Yuan Zheng(郑远), Yi Yin(尹艺), Yang Liu(刘洋), and Xiaofeng Xu(许晓峰)

Citation: Chin. Phys. B, 2026, 35 (**6**): 067103. DOI: 10.1088/1674-1056/ae0b45
http://cpb.iphy.ac.cn; http://iopscience.iop.org/cpb

What follows is a list of articles you may be interested in

Synthesis, structure and physical properties of ternary Ce-based compound Ce_3VAs_5

B S Min(闵保森), L C Fu(傅立承), X M Chen(陈晓铭), L C Shi(史鲁川), H Y Zheng(郑皓宇), J Zhang(张俊), J Song(宋静), Z Deng(邓正), J F Zhao(赵建发), L Duan(段磊), C J Xiao(肖长江), J L Zhu(朱金龙), X C Wang(望贤成), and C Q Jin(靳常青)

Chin. Phys. B, 2026, 35 (**5**): 057111. DOI: 10.1088/1674-1056/ae1ded

Photoexcitation of the one-dimensional extended Peierls-Hubbard model at quarter-filling

Yu-Peng Li(李昱澎), Yu-Chang Liu(刘羽畅), Yu-Zhuo Zhao(赵玉卓), Hantao Lu(陆汉涛), and Can Shao(邵灿)

Chin. Phys. B, 2026, 35 (**5**): 057104. DOI: 10.1088/1674-1056/ae27af

Electronic structure study of the intermetallic compound $GdRhIn_5$

Yulu He(贺宇璐), Bo Wang(王博), Xiangfei Yang(杨向飞), Dengpeng Yuan(袁登鹏), Wei Feng(冯卫), Yaobo Huang(黄耀波), and Qiuyun Chen(陈秋云)

Chin. Phys. B, 2026, 35 (**3**): 037101. DOI: 10.1088/1674-1056/ae3123

Numerical study of a quantum spin in an s-wave superconductor using the natural orbitals renormalization group method

Wen-Jing Zhang(张文静), Ru Zheng(郑汝), Rong-Qiang He(贺荣强), and Zhong-Yi Lu(卢仲毅)

Chin. Phys. B, 2026, 35 (**2**): 027104. DOI: 10.1088/1674-1056/adf4af

Realization of low-energy type-Ⅱ Dirac fermions in $(Ir_{1-x}Pt_x)Te_2$ superconductors

Bin-Bin Fu(付彬彬), Chang-Jiang Yi(伊长江), Zhi-Jun Wang(王志俊), Meng Yang(杨萌), Bai-Qing Lv(吕佰晴), Xin Gao(高鑫), Man Li(李满), Yao-Bo Huang(黄耀波), Hong-Ming Weng(翁红明), You-Guo Shi(石友国), Tian Qian(钱天), Hong Ding(丁洪)

Chin. Phys. B, 2019, 28 (**3**): 037103. DOI: 10.1088/1674-1056/28/3/037103

Moiré superlattice on the surface of Sm films driven by surface valence transition

Jianzhou Bian(边建州)[1,†], Hao Zheng(郑浩)[2,†], Yonghao Liu(刘永昊)[3], Zongxiu Wu(邬宗秀)[3], Yuan Zheng(郑远)[3], Yi Yin(尹艺)[3,‡], Yang Liu(刘洋)[2,§], and Xiaofeng Xu(许晓峰)[1,¶]

[1] *School of Physics, Zhejiang University of Technology, Hangzhou* 310023, *China*
[2] *Center for Correlated Matter and School of Physics, Zhejiang University, Hangzhou* 310058, *China*
[3] *Zhejiang Province Key Laboratory of Quantum Technology and Device, School of Physics, Zhejiang University, Hangzhou* 310027, *China*

(Received 27 May 2025; revised manuscript received 25 August 2025; accepted manuscript online 25 September 2025)

Rare earth (RE) metals exhibit unique mixed-valence behavior due to their 4f electronic configurations. In this study, we investigate the surface electronic structure and valence-mixing phenomena in samarium (Sm) films using molecular beam epitaxy (MBE), scanning tunneling microscopy (STM), angle-resolved photoemission spectroscopy (ARPES), and density functional theory (DFT). A natural moiré superlattice emerges on the Sm film surface as a result of lattice mismatch between the surface divalent Sm^{2+} and bulk trivalent Sm^{3+} layers. ARPES reveals the flat f electron bands corresponding to Sm^{3+} and Sm^{2+} states, particularly demonstrating the partial coexistence of bulk Sm^{2+} flat bands. The dispersive s–d electron bands and surface-condition-induced band shifts are observed and analyzed through both STM and ARPES measurements. Our work provides direct evidence for the formation of a moiré pattern on the surface of Sm films due to its unique surface valence transition, thus paving the way for a new method to generate moiré superlattices in correlated 4f-electron systems.

Keywords: samarium, mixed valence, angle-resolved photoelectron spectroscopy, scanning tunneling microscopy

PACS: 71.27.+a, 79.60.–i, 68.37.Ef, 73.20.At

DOI: 10.1088/1674-1056/ae0b45 **CSTR:** 32038.14.CPB.ae0b45

1. Introduction

Rare earth (RE) materials with 4f electrons are renowned for their strong electronic correlations, which can give rise to a variety of intriguing quantum phenomena, including heavy fermion behavior, magnetic order, mixed valence, unconventional superconductivity, and quantum criticality.[1–8] Due to the relatively low energy scales, these systems are highly sensitive to external tuning parameters such as doping, pressure, and magnetic field. In RE materials, the valence is defined as the number of electrons donated by each RE ion to the 5d–6s conduction band. Among the lanthanides, most elements prefer a trivalent (3+) ground state; however, several elements with near half-filled or fully filled 4f shells (*e.g.*, Eu and Yb) tend to exhibit divalent (2+) states more readily.[9] For samarium (Sm), due to the relatively small energy difference between Sm^{2+} and Sm^{3+}, it often displays mixed-valence behavior. Its valence can be tuned between these two states by applying pressure, adjusting temperature, and chemical doping, giving rise to a range of intriguing phenomena.[4,10]

Early studies have demonstrated that bulk Sm predominantly exhibits a trivalent (Sm^{3+}) electronic configuration, whereas its surface atoms are more likely to adopt a divalent (Sm^{2+}) state. This leads to a pronounced valence transition in the outermost layer.[11–13] The larger ionic radius of Sm^{2+} can result in an incommensurate interface with the compact Sm^{3+} layers, thereby inducing surface reconstruction and the spontaneous formation of a superlattice with large periodicity (or moiré pattern).[14,15]

Moiré lattices have garnered significant attention in recent years.[16–19] In a moiré system, the enlarged supercell can lead to substantial band flattening due to band folding, thereby enhancing the effects of even relatively weak electron–electron interactions. Such correlation effects have been experimentally demonstrated across various moiré systems, where intriguing phenomena — ranging from correlated insulators and fractional Chern insulators to superconductivity — have been observed.[20–22] Generally, moiré lattices can be realized by introducing a small twist angle between two layered materials or by stacking structurally similar materials with different lattice constants; however, these methods often present considerable challenges in terms of fabrication and scalability. In

[†]These authors contributed equally to this work.
[‡]Corresponding author. E-mail: yiyin@zju.edu.cn
[§]Corresponding author. E-mail: yangliuphys@zju.edu.cn
[¶]Corresponding author. E-mail: xuxiaofeng@zjut.edu.cn

© 2026 Chinese Physical Society and IOP Publishing Ltd. All rights, including for text and data mining, AI training, and similar technologies, are reserved.

contrast, in rare-earth metals with surface valence transitions, the lattice change associated with the valence transition can induce the formation of a moiré superlattice, offering an attractive and potentially more accessible platform for investigating moiré physics in a strongly correlated setting.

However, most prior studies have relied on x-ray photoemission spectroscopy (XPS) or angle-integrated photoemission spectroscopy (PES).[11–13] The precise nature of the surface valence transition and its impact on the conduction states remain largely unexplored, particularly in the context of Sm films exhibiting a well-defined moiré pattern. Therefore, high-resolution spectroscopic measurements in both real and momentum space are essential for understanding the characteristics of Sm's surface valence transition. In this work, we combine molecular beam epitaxy (MBE), *in-situ* scanning tunneling microscopy (STM), *in-situ* angle-resolved photoemission spectroscopy (ARPES), and density functional theory (DFT) calculations to address these questions. The moiré pattern resulting from the lattice mismatch between surface Sm^{2+} and bulk Sm^{3+} is distinctly observed in STM measurements. ARPES reveals f electron multiplets originating from both surface Sm^{2+} and bulk Sm^{3+} states. Furthermore, a partial bulk Sm^{2+} state is found to coexist dynamically with the predominant bulk Sm^{3+} state. We further analyze the dispersive s–d electron conduction bands and their shifts induced by surface effects. The combination of these techniques facilitates a comprehensive examination of both the mixed-valence phenomenon and the distinction between surface and bulk states.

2. Experiment and results

Figure 1(a) presents a schematic representation of the lattice structure of bulk Sm, characterized by a nine-layer close-packed arrangement. Each layer of Sm(001) exhibits a triangular lattice with an in-plane lattice constant of 0.363 nm, while the interlayer spacing between adjacent layers is 0.291 nm. The side and top views illustrate that the lattices in different layers are stacked in an alternating sequence, designated as Sm_A, Sm_B, and Sm_C. The MBE growth process began with the preparation of a bilayer graphene substrate, which was achieved by annealing an Si-terminated 6H-SiC(0001) substrate at 1300 °C for 30 minutes under ultra-high-vacuum (UHV) conditions (4×10^{-10} Torr, 1 Torr = 1.33322×10^2 Pa). The quality of the resulting epitaxial graphene layer was evaluated using reflection high-energy electron diffraction (RHEED), which also served as the foundation for the subsequent epitaxial growth of Sm films. Subsequently, 2-unit-cell-thick Sm films (equivalent to 18 monolayers) were epitaxially deposited under conditions of a deposition rate of 0.914 Å/min and an Sm source temperature maintained at 540 °C. Both film thickness and deposition rate were precisely controlled using an *in-situ* quartz crystal microbalance (QCM). The substrate was maintained at room temperature during the film deposition process. Upon completion of the thin film growth, the samples were annealed at 150 °C for 5 minutes to enhance both film quality and surface flatness. Figure 1(b) displays the RHEED pattern for Sm along the Γ–M direction. The presence of sharp streaks, whose in-plane lattice constant is consistent with bulk Sm, confirms the high surface quality attained in these Sm films.

The sample was subsequently transferred *in-situ* to the STM head for measurement at liquid nitrogen temperature (77 K). Figure 1(c) displays a large-scale STM topographic image acquired with a bias voltage of $V_b = 1$ V and a set-point tunneling current of $I_t = 200$ pA. Triangular terraces with periodic lattices are observable; however, the surface is rough with multiple terraces at varying heights. The sample was then transferred to the preparation chamber at room temperature, re-annealed at 150 °C for 5 minutes, and subsequently returned to the low-temperature STM head for further measurements. As shown in Fig. 1(d), the surface morphology becomes relatively smoother following this annealing process. Two line-cuts across the steps depicted in Fig. 1(d) have been selected, and the corresponding step heights are extracted as shown in Fig. 1(e). The top panel (along the red cut in panel (d)) corresponds to the height of a single Sm lattice layer, while the bottom panel (along the light blue cut in panel (d)) represents two unit cells comprising 18 layers of the Sm lattice (with graphene located beneath this step). The surface was predominantly covered by Sm layers with a height of 2 unit cells (u.c.), consistent with the overall thickness estimated by the QCM.

Figure 1(f) presents a topographic image of a small flat surface, revealing a clearly defined periodic triangular lattice. The real-space lattice exhibits a period that is significantly larger than the atomic scale, suggesting the possibility of surface reconstruction. The Fourier transform of Fig. 1(f), shown in the top right corner, allows for the precise determination of the superlattice period as 1.916 nm. In a previous STM study,[15] a similar reconstruction was observed, with its period being approximately 4.5 times that of the surface atomic lattice. The lack of atomic resolution in our experiment may be attributed to the tip treatment, where an extremely sharp tip was intentionally avoided to ensure accurate spectroscopic measurements. The RHEED pattern also displays prominent superstructure peaks. Figure 1(b) depicts the intensity profile along a horizontal line-cut across the RHEED streaks, enabling the extraction of both the distance between two primary peaks (λ_2) and the distance between primary and secondary peaks (λ_1). Based on the calculated value of λ_2/λ_1, the period of the surface superstructure along this direction is determined to be approximately 4.35 times that of the atomic periodicity.

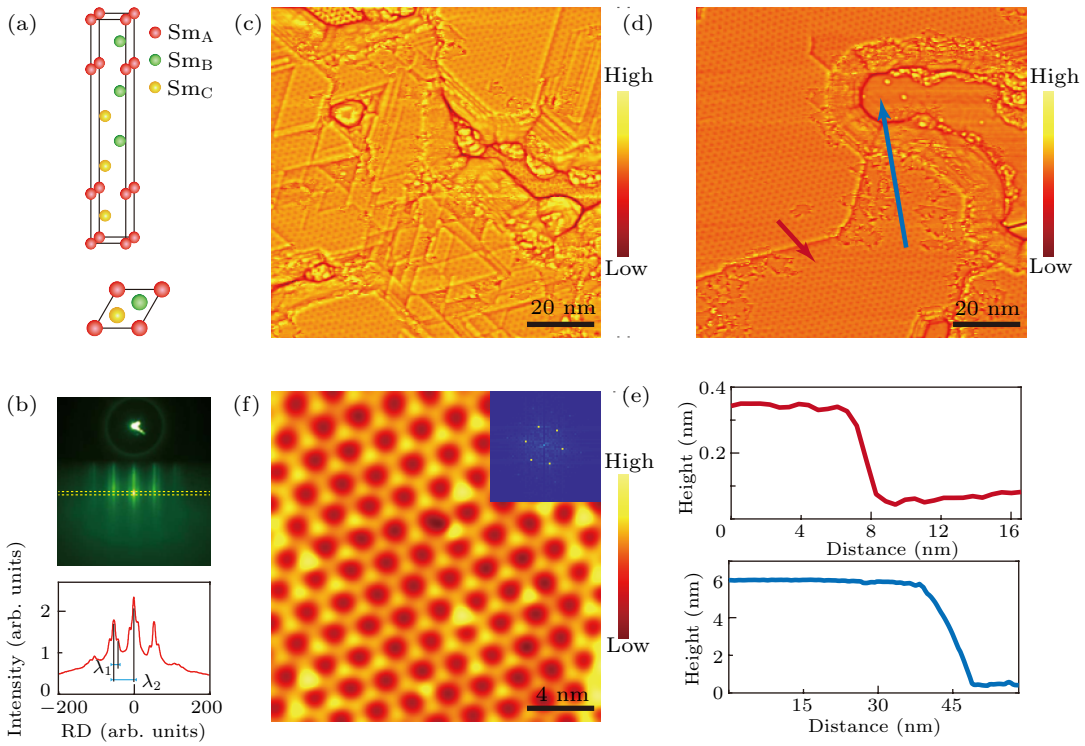


Fig. 1. (a) Crystal structure of bulk Sm. The side view and top view sketches are presented in the upper and lower panels, respectively. (b) Top: RHEED pattern of an Sm film for electron beam along the Γ–M direction. Bottom: RHEED line-cut along the yellow dashed box. (c)–(d) Large-scale topography ($V_b = 1$ V, $I_t = 200$ pA) of the Sm film after annealing at 150 °C and after re-annealing (d). (e) Height profiles corresponding to the colored arrowed lines indicated in panel (d). (f) Topography of a region exhibiting a flat surface. The inset displays the Fourier transformation results. All STM measurements were conducted at liquid nitrogen temperature (77 K).

The center of the reconstructed superlattice is characterized by a dark spot, surrounded by a bright hexagon, which aligns with earlier findings reported in the literature.[15] The amplitude of modulation observed in the topography is approximately 20 pm in our experiment. This reconstruction can be modeled as a moiré pattern arising from a lattice mismatch between the surface divalent Sm^{2+} lattice and the underlying bulk trivalent Sm^{3+} lattice.[15] We note that RE metals can be viewed as a lattice of RE ions with a specific valence (corresponding to the number of conduction electrons that are donated to the Fermi sea), which coexists with the itinerant conduction electrons. Each dark spot corresponds to a depressed surface atom of divalent Sm^{2+}, occurring when it is directly positioned above a trivalent Sm^{3+} atom in the layer beneath. Typically, bulk Sm exists predominantly in its trivalent state (Sm^{3+}). However, on the surface, Sm tends to adopt a divalent state (Sm^{2+}) due to a reduction in coordination number and the effects of lattice termination. The atomic radius of divalent Sm^{2+} is larger than that of its trivalent counterpart (Sm^{3+}). Regardless of stacking order, these two incommensurate layers exhibiting lattice mismatch lead to the formation of a moiré superlattice. In our experiment, with a lattice constant of 0.363 nm for bulk Sm^{3+}, we observe that the periodicity of 1.916 nm corresponds to an average spacing involving 5.28 trivalent Sm^{3+} atoms interspersed between two neighboring surface dark spots. The moiré periodicity induced by this lattice mismatch suggests an average presence of 4.28 divalent surface Sm^{2+} atoms located between two dark spots, which is approximately consistent with the periodicity observed in RHEED. Therefore, the STM findings reveal that the atomic radius of surface Sm expands by approximately 23% compared to bulk trivalent Sm^{3+}.

We concentrated on a small, flat region characterized by the topography depicted in Fig. 2(a) ($V_b = 1$ V, $I_t = 200$ pA). The STM tip was positioned at the center of a dark spot within this topography (indicated by the blue dot). A differential conductance (dI/dV) spectrum was subsequently acquired within the bias range of ± 600 mV and is presented in Fig. 2(b). For the dI/dV spectrum measurement, a standard lock-in technique was employed, utilizing a voltage modulation of 10 mV and a frequency of 991.2 Hz. For comparison, an additional dI/dV spectrum was measured at the location of a bright spot (indicated by the red dot) and is also presented in Fig. 2(b). The most prominent feature observed in both spectra is a broad peak that extends from zero bias (the Fermi level) to a positive bias of 600 mV (above the Fermi level). Notably, there is a slight shift in the peak center, moving from 380 mV for the bright spot to 320 mV for the dark spot.

To gain a deeper understanding of the experimental bands near the Fermi level, we performed first-principles calculations using the Vienna *Ab-initio* Simulation Package (VASP).[23] The Perdew–Burke–Ernzerhof (PBE) exchange–correlation functional[24] was employed within the framework of the projector-augmented wave (PAW) method.[25] We uti-

lized the "Sm_3" pseudopotential in our calculation, which assumes a $4f^5$ configuration for Sm with 4f electrons treated as core electrons (hence not part of the band structure). Due to technical limitations, both the 4f electrons and the structure of the moiré surface were omitted from our band calculation. Additional details regarding the DFT calculations are provided in Appendix A.

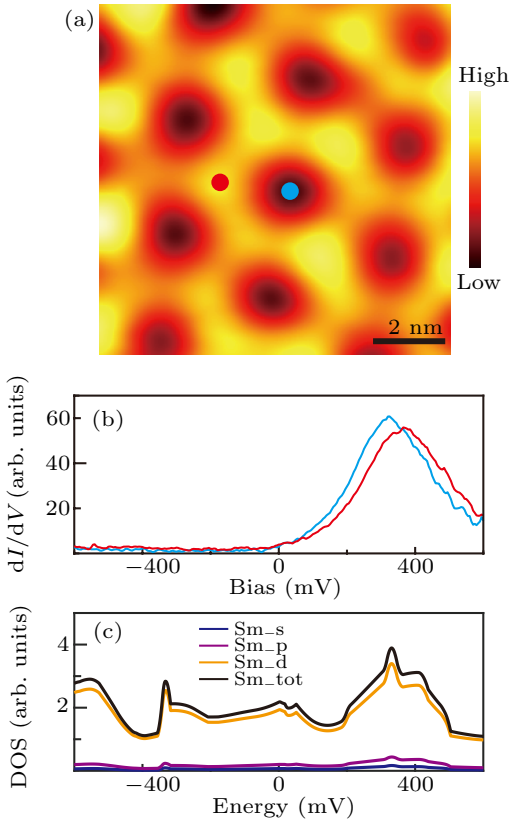


Fig. 2. (a) Topography of a small flat region ($V_b = 1$ V, $I_t = 200$ pA). (b) The two dI/dV spectra measured at the corresponding points indicated in panel (a). These spectra were collected using the standard lock-in technique with a voltage modulation of 10 mV and a frequency of 991.2 Hz. (c) Calculated projected density of states (DOS) near the Fermi level for Sm. The Sm 4f electrons are not taken into account in the calculation.

Figure 2(c) presents the calculated projected density of states (DOS) near the Fermi level for Sm. As shown in Fig. 2(c), it is evident that the DOS for conduction electrons is predominantly attributed to Sm 5d electrons close to the Fermi level. A pronounced peak around 350 mV can be observed, aligning with features noted in dI/dV spectra. In contrast, certain features below the Fermi level are absent from the STM spectra. A detailed analysis of the band structure indicates that this peak at 350 mV corresponds to the bottom of several electronic pockets situated above the Fermi level; meanwhile, the DOS below the Fermi level is associated with 5d hole pockets as further demonstrated in Fig. 4(b). Due to an unknown origin, the hole pocket bands are not detected in STM measurements, which is indicative of a small tunneling matrix element. When the tip is positioned at the center of the moiré pattern, a lower apparent height indicates closer proximity to the underlying bulk state, which is associated with a preference for trivalent behavior and thereby enhances the contributions from 5d conduction electrons. Consequently, this results in a shift of the Fermi level towards higher energy, consistent with the 60-mV downward shift observed for the 5d peak, as shown in Fig. 2(b).

In a separate UHV system, an Sm film with a thickness of two unit cells was grown under a similar recipe. The sample was then transferred *in-situ* to the ARPES chamber for electronic structure measurements ($\sim$ 6 K). Figure 3(a) presents ARPES results over a broad energy range obtained using 40.8-eV photon energy (He II), which effectively probes the 4f states. The energy distribution curve (EDC) depicted in Fig. 3(b) was derived by integrating the entire spectrum. In Fig. 3(a), the three strongest non-dispersive flat bands are distinctly observed at -0.9 eV, -1.7 eV, and -5.2 eV, respectively. These bands correspond to the three prominent peaks identified in the EDC shown in Fig. 3(b). In addition, two weak flat bands (or corresponding peaks) are observed around -4.0 eV, and another two weak flat bands (or corresponding peaks) appear below -7.0 eV. These features can be directly attributed to localized 4f electrons within ionic cores, which accounts for their relative absence in STM measurements.[26–29] The flat bands extending from the Fermi level down to -4.5 eV are ascribed to the Sm^{2+} at surface, corresponding to the $4f^5$ final state (resulting from ionization of one electron from the $4f^6$ configuration). Below this energy range, contributions from the bulk Sm^{3+} state ($4f^4$ final state) dominate, with 4f multiplets corresponding to Sm^{3+} ranging from -10.0 eV to -4.5 eV. The energy difference between the Sm^{2+} and Sm^{3+} states reflects strong correlation effects among 4f electrons, which requires a large Coulomb energy when an extra electron is incorporated into the system. For the Sm^{2+} components, three faint peaks are discernible near the Fermi level as indicated by three black vertical lines in Fig. 3(b). The origins of these faint peaks will be revisited in the subsequent discussion.

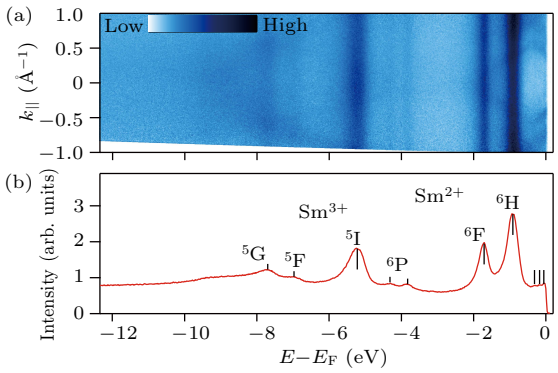


Fig. 3. (a) Wide-range photoemission data taken by He II photons (40.8 eV) and (b) corresponding energy distribution curve (EDC) of an Sm thin film. The ARPES measurements were conducted at approximately 6 K. The multiple flat bands observed from -4.5 eV to -10.0 eV correspond to the 4f bands associated with trivalent Sm, whereas the flat bands extending from the Fermi level (E_F) to -4.5 eV are attributed to the 4f bands of divalent Sm.

We observe several dispersive bands below the Fermi level. To gain a more comprehensive understanding of the band dispersion characteristics in Sm, high-resolution scans were conducted in the vicinity of the Fermi level. Here the intense 4f electronic signal at −0.9 eV overwhelms the weak conduction electron bands near the Fermi level, regardless of whether He I (21.2 eV) or He II (40.8 eV) photon energies are employed. Within the measured momentum range, both photon energy conditions exhibit similar dispersion behaviors, suggesting a quasi-two-dimensional nature of the Sm bands. Given that He II photon energy reveals clearer dispersion features near the Fermi level, subsequent analyses primarily focus on the He II spectra.

Figure 4(a) presents the high-resolution ARPES spectrum measured along the Γ–M direction. In proximity to the Fermi surface, the electronic structure reveals three flat bands located at 0 eV, −0.17 eV, and −0.32 eV, alongside three hole-like bands designated as α, β, and γ. The three flat bands near the Fermi level are also indicated by three short vertical lines in Fig. 3(b). By comparing the 4f spectra from Sm-based compounds in the literature,[26] we can assign these three flat bands as the $^6H_{5/2}$, $^6H_{7/2}$, and $^6H_{9/2}$ multiplets of the $4f^5$ state. Their intensity is small because the bulk Sm^{2+} component in Sm is weak. By contrast, the intense peaks at −0.9 eV and −1.7 eV can be assigned to ^{6}H and ^{6}F states for the surface Sm^{2+} — its strong intensity proves that the Sm on the top layer is mainly 2+. Due to a distinct chemical environment, it is anticipated that the surface ^{6}H state will shift to lower energy compared to its bulk counterpart,[26,30–32] leading to the observed peak at −0.9 eV. Concurrently, a bulk ^{6}F state may be embedded within this peak at −0.9 eV. The surface ^{6}F state shifts further down in energy, resulting in a peak at −1.7 eV. Consequently, we assign the two distinct peaks observed at −0.9 eV and −1.7 eV to the surface ^{6}H and ^{6}F states, respectively, as illustrated in Fig. 3(b). The two weak flat bands located around −4.0 eV correspond to the ^{6}P multiplets.[30] The flat band observed at −5.2 eV can be attributed to the ^{5}I peak arising from the bulk Sm^{3+} state, while the two weak flat bands below −7.0 eV are assigned to the ^{5}F and ^{5}G multiplets.[30]

Despite the surface reconstruction confirming the coexistence of surface Sm^{2+} and bulk Sm^{3+} states, a residual contribution from bulk Sm^{2+} (green arrows in Fig. 4(a)) can be identified in ARPES measurements. The bulk Sm^{2+} signal is very weak because bulk Sm is mostly in Sm^{3+} with a very small Sm^{2+} contribution, and the bulk Sm is buried beneath the top layer. The coexistence of bulk Sm^{2+} and Sm^{3+} exhibits rapid dynamic variations over time, resulting in a slight deviation of the bulk valence from 3+. Therefore, we have a unique scenario of a surface moiré pattern in Sm driven by the surface valence change, distinct from a purely structural change in previously reported moiré systems. In SmB_6, the strong Sm^{2+} component in bulk leads to strong valence mixing and hybridization between 4f and conduction electrons.[33–35] Conversely, in metallic Sm, the predominance of the bulk Sm^{3+} state leads to weaker hybridization between 4f and conduction bands (Fig. 4(b)).

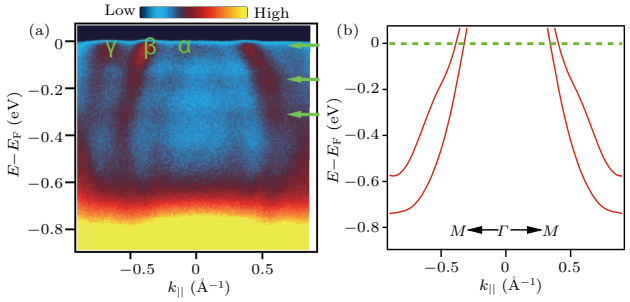


Fig. 4. (a) Band structure near the Fermi level taken by He II photons (40.8 eV) and (b) comparisons with first-principles calculations at $k_z = 0$. Here the flat bands near E_F in panel (a) (marked by green arrows) are Sm 4f bands, which are not taken into account in the calculation of panel (b).

In the DFT calculations, the primitive unit cell of Sm (rhombohedral structure) was employed for the computations, and the band structure was projected onto the (001) direction of the conventional hexagonal unit cell. Notably, the calculations predict only two hole-like bands near the Γ point for all k_z planes along the Γ–M direction (Appendix A and Fig. A1); however, our experiments identify three bands (α, β, γ). Both the β and γ bands exhibit stronger intensities compared to the weaker α band. A possible explanation for this phenomenon is that modifications to the surface valence induce doping effects in the conduction bands of the outermost Sm atoms, resulting in a relative band shift with respect to the bulk states. The strong experimental signals corresponding to the β and γ bands may be attributed to these shifted surface states, whereas the weaker α and a hidden β' band could correspond to the two bulk state bands. The hidden β' band may overlap with β and is therefore indistinguishable from it. Future high-resolution measurements and a more detailed comparison with calculations may further clarify the origin of the bands.[36]

3. Conclusion

In conclusion, we present a comprehensive spectroscopic investigation of Sm films with a valence transition at the surface. A triangular moiré superlattice forms on the surface of the Sm film due to lattice mismatch between the surface Sm^{2+} layer (expanded by 23% relative to bulk Sm^{3+}) and the subsurface Sm^{3+} layer. In addition to the flat bands associated with bulk Sm^{3+} and surface Sm^{2+}, ARPES also identifies flat bands originating from localized $4f^5$ states of bulk Sm^{2+}. The surface Sm^{2+} state exhibits a core-level shift of approximately 0.9 eV relative to the bulk Sm^{2+} state. These multiple flat bands arise from multiplet configurations corresponding to different final $4f^5$ states. Dispersive conduction bands near

the Fermi level and their spectroscopic shifts are systematically investigated using both STM and ARPES measurements. Further investigation may require the utilization of advanced synchrotron radiation light sources with nano-ARPES to systematically explore potential flat bands within the folded mini Brillouin zone.[37,38] Our combined STM and ARPES study provides a compelling case that interfacial moiré systems can be created by surface valence transitions in rare-earth systems, which are quite common in these systems. Our work therefore opens up new opportunities to search for moiré superlattices in 4f-electron systems and other correlated systems.

Appendix A: Details of DFT calculations

All DFT calculations were carried out using VASP within the PBE generalized-gradient approximation and the PAW framework. Samarium was modeled using the "Sm_3" pseudopotential, in which the 4f electrons are treated as core states. This choice focuses on the conduction bands near the Fermi level (E_F), which are predominantly composed of Sm-5d states, while the localized 4f multiplets are investigated through experimental analysis.

Self-consistent and DOS calculations employed the primitive rhombohedral bulk cell with lattice parameters $a = b = c = 8.991722$ Å and $\alpha = \beta = \gamma = 23.278233°$. A Monkhorst–Pack grid of $6 \times 6 \times 6$ and a plane-wave cutoff energy of 550 eV were used. For comparison with ARPES measured on the (001) plane of the conventional hexagonal cell ($a = b = 3.6281$ Å, $c = 26.233$ Å, $\alpha = \beta = 90°$, $\gamma = 120°$), the band dispersions from the primitive cell were projected onto the Γ–M direction of the hexagonal (001) plane. To investigate the potential out-of-plane dispersion, we analyzed the Γ–M bands across multiple k_z values ranging from 0 to π, with increments of 0.1π, as illustrated in Fig. A1.

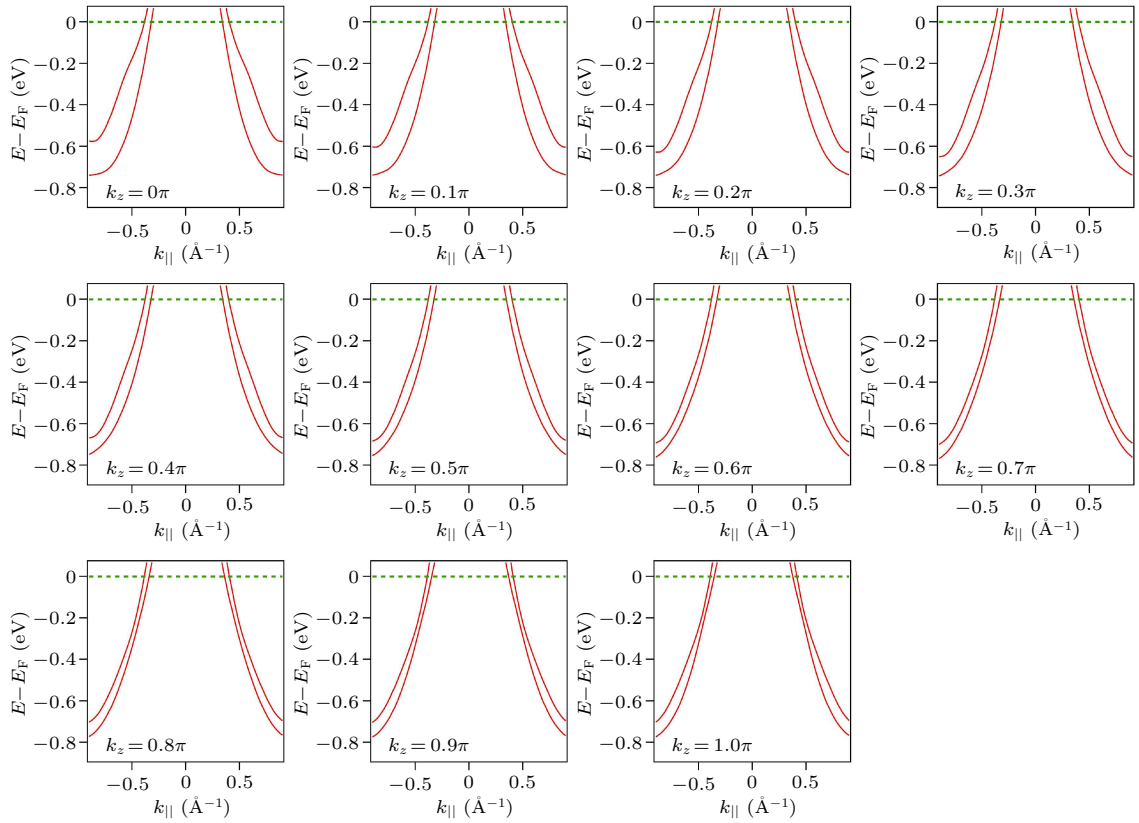


Fig. A1. The k_z-resolved DFT band structures near E_F of Sm along Γ–M direction.

Acknowledgements

Project supported by the National Key Research and Development Program of China (Grant Nos. 2022YFA1403202 and 2022YFA1402200), the National Natural Science Foundation of China (Grant Nos. 12174331 and 12274369), and the Zhejiang Provincial Natural Science Foundation of China (Grant No. LZ25A040003).

References

[1] Coleman P 2007 *Heavy Fermions: Electrons at the Edge of Magnetism, Handbook of Magnetism and Advanced Magnetic Materials*, eds. Kronmüller H and Parkin S, Vol. 1: *Fundamentals and Theory* (Chichester: Wiley) pp. 1–54
[2] Gegenwart P, Si Q and Steglich F 2008 *Nat. Phys.* **4** 186
[3] Kirchner S, Paschen S, Chen Q, Wirth S, Feng D, Thompson J D and Si Q 2020 *Rev. Mod. Phys.* **92** 011002
[4] Varma C M 1976 *Rev. Mod. Phys.* **48** 219
[5] Lawrence J M, Riseborough P S and Parks R D 1981 *Rep. Prog. Phys.* **44** 1
[6] Riseborough P S and Lawrence J M 2016 *Rep. Prog. Phys.* **79** 084501

[7] Chen Q Y, Xu D F, Niu X H, Jiang J, Peng R, Xu H C, Wen C H P, Ding Z F, Huang K, Shu L, Zhang Y J, Lee H, Strocov V N, Shi M, Bisti F, Schmitt T, Huang Y B, Dudin P, Lai X C, Kirchner S, Yuan H Q and Feng D L 2017 *Phys. Rev. B* **96** 045107

[8] Yuan Y H, Duan Y X, Rusz J, Zhang C, Song J J, Wu Q Y, Sassa Y, Tjernverg O, Månsson M, Berntsen M H, Wu F Y, Liu S Y, Liu H, Zhu S X, Liu Z T, Zhao Y Z, Tobash P H, Bauer E D, Thompson J D, Oppeneer P M, Durakiewicz T and Meng J Q 2021 *Phys. Rev. B* **103** 125122

[9] Strange P, Svane A, Temmerman W, Szotek Z and Winter H 1999 *Nature* **399** 756

[10] Higashinaka R, Yamada A, Matsuda T D and Aoki Y 2018 *AIP Advances* **8** 125017

[11] Wertheim G K and Crecelius G 1978 *Phys. Rev. Lett.* **40** 813

[12] Allen J W, Johansson L I, Lindau I and Hagstrom S B 1980 *Phys. Rev. B* **21** 1335

[13] Rosengren A and Johansson B 1982 *Phys. Rev. B* **26** 3068

[14] Stenborg A, Andersen J N, Björneholm O, Nilsson A and Mårtensson N 1989 *Phys. Rev. Lett.* **63** 187

[15] Lundgren E, Andersen J N, Nyholm R, Torrelles X, Rius J, Delin A, Grechnev A, Eriksson O, Konvicka C, Schmid M and Varga P 2002 *Phys. Rev. Lett.* **88** 136102

[16] He F, Zhou Y, Ye Z, Cho S, Jeong J, Meng X and Wang Y 2021 *ACS Nano* **15** 5944

[17] Lau C N, Bockrath M W, Mak K F and Zhang F 2022 *Nature* **602** 41

[18] Mak K F and Shan J 2022 *Nat. Nanotechnol.* **17** 686

[19] Nuckolls K P and Yazdani A 2024 *Nat. Rev. Mater.* **9** 460

[20] Cao Y, Fatemi V, Fang S, Watanabe K, Taniguchi T, Kaxiras E and Jarillo-Herrero P 2018 *Nature* **556** 43

[21] Park H, Cai J, Anderson E, Zhang Y, Zhu J, Liu X, Wang C, Holtzmann W, Hu C, Liu Z, Taniguchi T, Watanabe K, Chu J, Cao T, Fu L, Yao W, Chang C, Cobden D, Xiao D and Xu X 2023 *Nature* **622** 74

[22] Xu F, Sun Z, Jia T, Liu C, Xu C, Li C, Gu Y, Watanabe K, Taniguchi T, Tong B, Jia J, Shi Z, Jiang S, Zhang Y, Liu X and Li T 2023 *Phys. Rev. X* **13** 031037

[23] Kresse G and Hafner J 1993 *Phys. Rev. B* **47** 558

[24] Perdew J P, Burke K and Ernzerhof M 1996 *Phys. Rev. Lett.* **77** 3865

[25] Kresse G and Joubert D 1999 *Phys. Rev. B* **59** 1758

[26] Denlinger J D, Allen J W, Kang J S, Sun K, Min B I, Kim D J and Fisk Z 2014 *JPS Conf. Proc.* **3** 017038

[27] Chikina A, Generalov A, Kummer K, Güttler M, Antonov V N, Kucherenko Y, Kliemt K, Krellner C, Danzenbächer S, Kim T, Dudin P, Geibel C, Laubschat C and Vyalikh D V 2017 *Phys. Rev. B* **95** 155127

[28] Yamaoka H, Thunström P, Jarrige I, Shimada K, Tsujii N, Arita M, Iwasawa H, Hayashi H, Jiang J, Habuchi T, Hirayama D, Namatame H, Taniguchi M, Murao U, Hosoya S, Tamaki A and Kitazawa H 2012 *Phys. Rev. B* **85** 115120

[29] Zheng H, Xiao Z, Pan Z, Yang G, Liu Y, Bian J, Wu Y, Hua T, Zhang J, Lu J, Li J, Sun T, Song Y, He R, Larrea Jiménez J, Cao G, Yuan H, Xu Y, Yin Y, Shi M, Cao C and Liu Y 2025 *Sci. China- Phys. Mech. Astron.* **68** 287511

[30] Wang P, Ni J F, Li H N, Zhang W H and Zhu J F 2008 *Surf. Sci.* **602** 3728

[31] Kaindl G, Höhr A, Weschke E, Vandré S, Schüßler-Langeheine C and Laubschat C 1995 *Phys. Rev. B* **51** 7920

[32] Tarasov A V, Glazkova D, Schulz S, Poelchen G, Kliemt K, Kraiker A, Muntwiler M, Laubschat C, Generalov A, Polley C, Krellner C, Vyalikh D V and Usachov D Y 2022 *Phys. Rev. B* **106** 155136

[33] Dzero M, Sun K, Galitski V and Coleman P 2010 *Phys. Rev. Lett.* **104** 106408

[34] Li L, Sun K, Kurdak C and Allen J W 2020 *Nat. Rev. Phys.* **2** 463

[35] Jiang J, Li S, Zhang T, Sun Z, Chen F, Ye Z R, Xu M, Ge Q Q, Tan S Y, Niu X H, Xia M, Xie B P, Li Y F, Chen X H, Wen H H and Feng D L 2013 *Nat. Commun.* **4** 3010

[36] Chatterjee S, Ruf J P, Wei H I, Finkelstein K D, Schlom D G and Shen K M 2017 *Nat. Commun.* **8** 852

[37] Lisi S, Lu X, Benschop T, de Jong T A, Stepanov P, Duran J R, Margot F, Cucchi I, Cappelli E, Hunter A, Tamai A, Kandyba V, Giampietri A, Barinov A, Jobst J, Stalman V, Leeuwenhoek M, Watanabe K, Taniguchi T, Rademaker L, van der Molen S J, Allan M P, Efetov D K and Baumberger F 2021 *Nat. Phys.* **17** 189

[38] Chen C, Nuckolls K P, Ding S, Miao W, Wong D, Oh M, Lee R L, He S, Peng C, Pei D, Li Y, Hao C, Yan H, Xiao H, Gao H, Li Q, Zhang S, Liu J, He L, Watanabe K, Taniguchi T, Jozwiak C, Bostwick A, Rotenberg E, Li C, Han X, Pan D, Liu Z, Dai X, Liu C, Bernevig B A, Wang Y, Yazdani A and Chen Y 2024 *Nature* **636** 342